

# Liquid Noble Detectors

Aksel Hallin  
GRIDS2019, TRIUMF





# What happens when charged particles pass through liquid noble detectors?

1. Ionization
2. Scintillation

Differences between nuclear recoils and electromagnetic interactions:

J A Nikkel et al 2012 JINST 7  
C03007

**Table 1.** Properties of Liquid Argon and Liquid Xenon in comparison to standard scintillators.

<i>Property</i>	<i>Argon</i>	<i>Xenon</i>	<i>NaI</i>	<i>Plastic (NE102 or equiv.)</i>
Atomic No. (Z)	18	54	46.5	5.6
Atomic weight (A)	39.95	131.3	(23/127)	(1/12)
Maximum recoil energy (% of incident n energy)	9.5	3.0	16/3 in NaI respectively	100/28 in H/C
Boiling point (K °)	87.3	165	> 300	> 300
Density (g/cc)	1.4	3.0	3.67	1.03
Electron mobility (cm <sup>2</sup> /v*s)	400	2200	n/a	n/a
Ion drift velocity at 1kV/cm (mm/ $\mu$ s)	2.2	2.4	n/a	n/a
Energy resolution (FWHM @ 662 keV) scint. only (%)	8%	8%	6.5%	$\approx$ 50%
Energy resolution, ionization+scintillation (%)	4 expected	4 (1.2 possible?)	(6.5)	$\approx$ 50
Scintillation wave length (nm) and PMT used	128 (w/ $\lambda$ shifter, fast PMT)	175 (quartz window PMT)	415 (regular PMT)	425 (fast PMT)
Scintillation yield (# scintillation photons/MeV)	40000	42000	38000	10000
Fast decay time (ns)	7 (25% light)	4.3	230	3
Slow decay time (ns)	1500 (75% light)	22(100% in $\leq$ 22ns)	n/a	n/a
(n, $\gamma$ ) propensity	medium	high	high	medium
Neutron activation	medium	high	high	none
Cost (\$/gram)	$\approx$ 0.002	$\approx$ 1.5	$\approx$ 0.5	$\approx$ 0.15

**Table 2.** Liquid noble gas physical properties including radioactivity.

Element	Z	A	Liquid density (g/cc)	Boiling point (K)	Photon yield ( $\gamma/\text{keV}$ )	Triplet decay time	Emission Wavelength (nm)	Radio activity
He	2	4.00	0.13	4.2	22	13(s)	80	None
Ne	10	20.18	1.2	27.1	32	15( $\mu\text{s}$ )	78	None
Ar	18	39.95	1.4	87.3	40	1.5( $\mu\text{s}$ )	128	<sup>39</sup> Ar 1Bq/kg
Kr	36	83.80	2.4	119.9	49	85(ns)	148	<sup>85</sup> Kr 1MBq/kg
Xe	54	131.30	3.1	165.0	64	22(ns)	175	<sup>136</sup> Xe < 10uBq/kg

# The DEAP 3600 Single Phase Detector

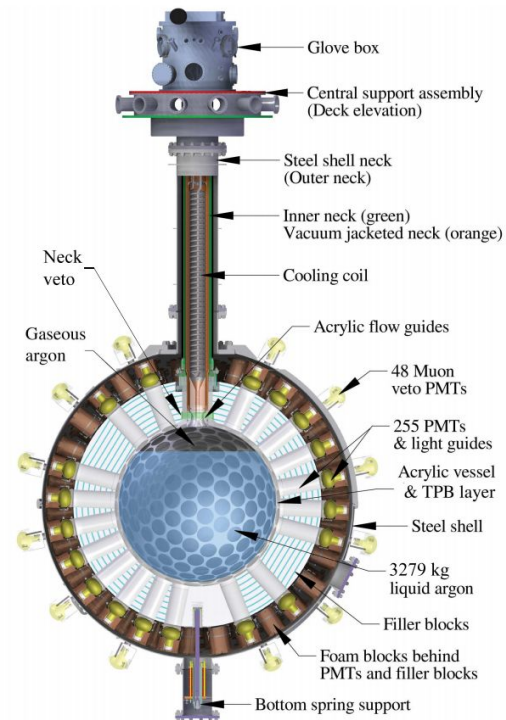
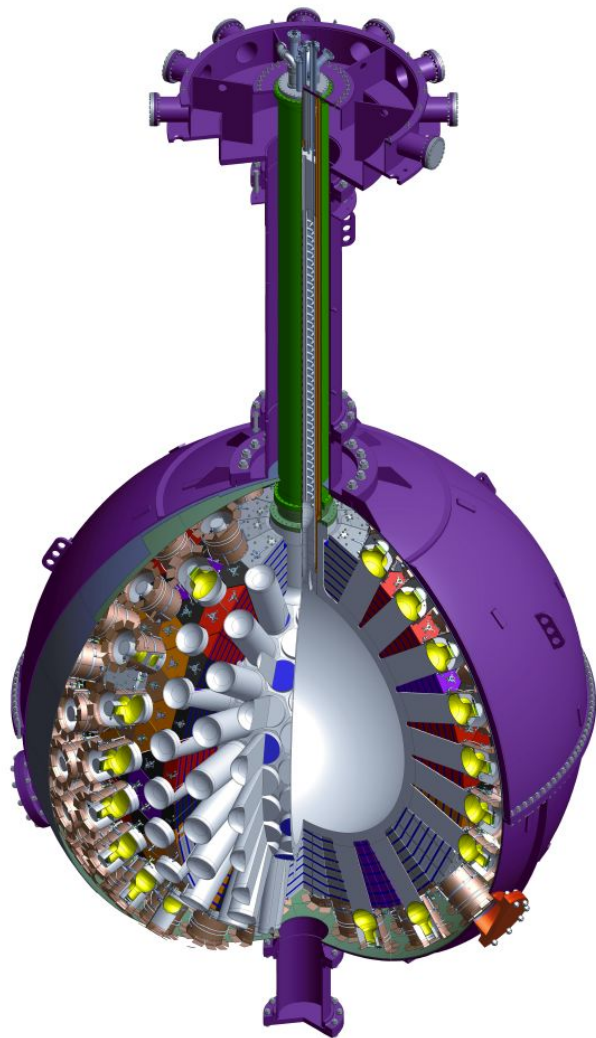


FIG. 1. Cross section of the DEAP-3600 detector components located inside the water tank (not shown). Inside the steel shell are inward-looking PMTs, light guides, filler blocks, and the acrylic vessel (AV), which holds the liquid argon target and the gaseous argon layer. Located on the outer surface of the steel shell are muon veto PMTs. Above this, a steel neck contains the neck of the AV, acrylic flowguides and the cooling coil. The neck is coupled to a central support assembly on which the glovebox is located. Shown also is the neck veto fiber system (green).

# Critical Elements of the Design

- Acrylic cryostat with lightguides and filler blocks.
  - Very low radioactivity (on order of ppt U and thorium)<sup>332</sup>
  - Good neutron moderator (requires 50 cm of acrylic to reduce neutrons from PMTs to background budget levels)
  - Good visible light transmission- moves the light from the ultraclean fiducial volume to the relatively “dirty” PMT’s/electronics/outer detector
  - Added bonus: thermal insulation is sufficient to allow use of room temperature PMT’s which are better understood than cryogenic PMTs. We need to understand PMT behaviour- especially light sources within PMTs at the level of one pulse/255 PMTs/3 years.
  - Note that the acrylic is structural: it provides mechanical support for itself (1Mg), the Lar(3.6 Mg), the lightguides and filler blocks ~ 10 Mg, the PMTs. It also withstands vacuum and pressure.
- Completely radon-tight inner volume that can be remotely resurfaced in a radon-controlled atmosphere and then sealed to prevent further exposure to airborne radon.
- Liquid argon active region
  - “Easily” purified (liquid noble)
  - Well defined and homogeneous background model
  - Exceptional PSD because of singlet (6 ns)/triplet (1.5  $\mu$ s) lifetime difference

# Acrylic Cryostat Design

- First/only large scale acrylic cryostat
- Measured mechanical (Young's modulus, tensile strength) properties of bonded and unbonded samples between room temperature and 87 K.
- Detailed finite element calculations of stresses due to thermal profile, gravity, pressure and supports. Decided to maintain a safety factor of 10 (a factor of 4 for bonds, and a "real" factor of 2.5).
- 5 cm shell thickness chosen to control thermal stress
- Stub design: light guide attachment done in low stress region
- Filler blocks: tolerances and freedom to move prevent stress transmission

# Fabrication and Assay of DEAP Acrylic

- Fabrication from pure MMA monomer at RPTAsia (Thailand), strict control of radon exposure for all steps
- DEAP Collaborators present during fabrication
- Control to  $< 10^{-20}$  g/g  $^{210}\text{Pb}$  from radon exposure
- Developed system to vaporize and assay large quantities of acrylic (10 kg samples), count residue with Ge well detector for  $^{210}\text{Pb}$  peak, and with alpha counter for  $^{210}\text{Po}$



Monomer cast at RPT Asia



Thermoformed Panel at RPT Colorado



The journey of the acrylic vessel begins in Thailand, where acrylic sheets are poured from clean acrylic monomer.

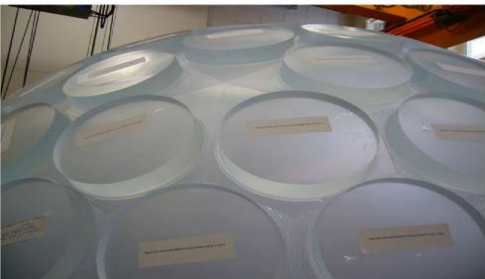
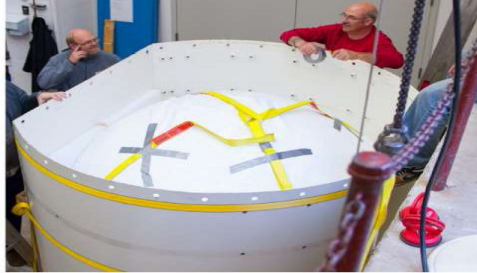


The sheets are thermoformed and machined into 'orange slices'.





The AV collar is machined.



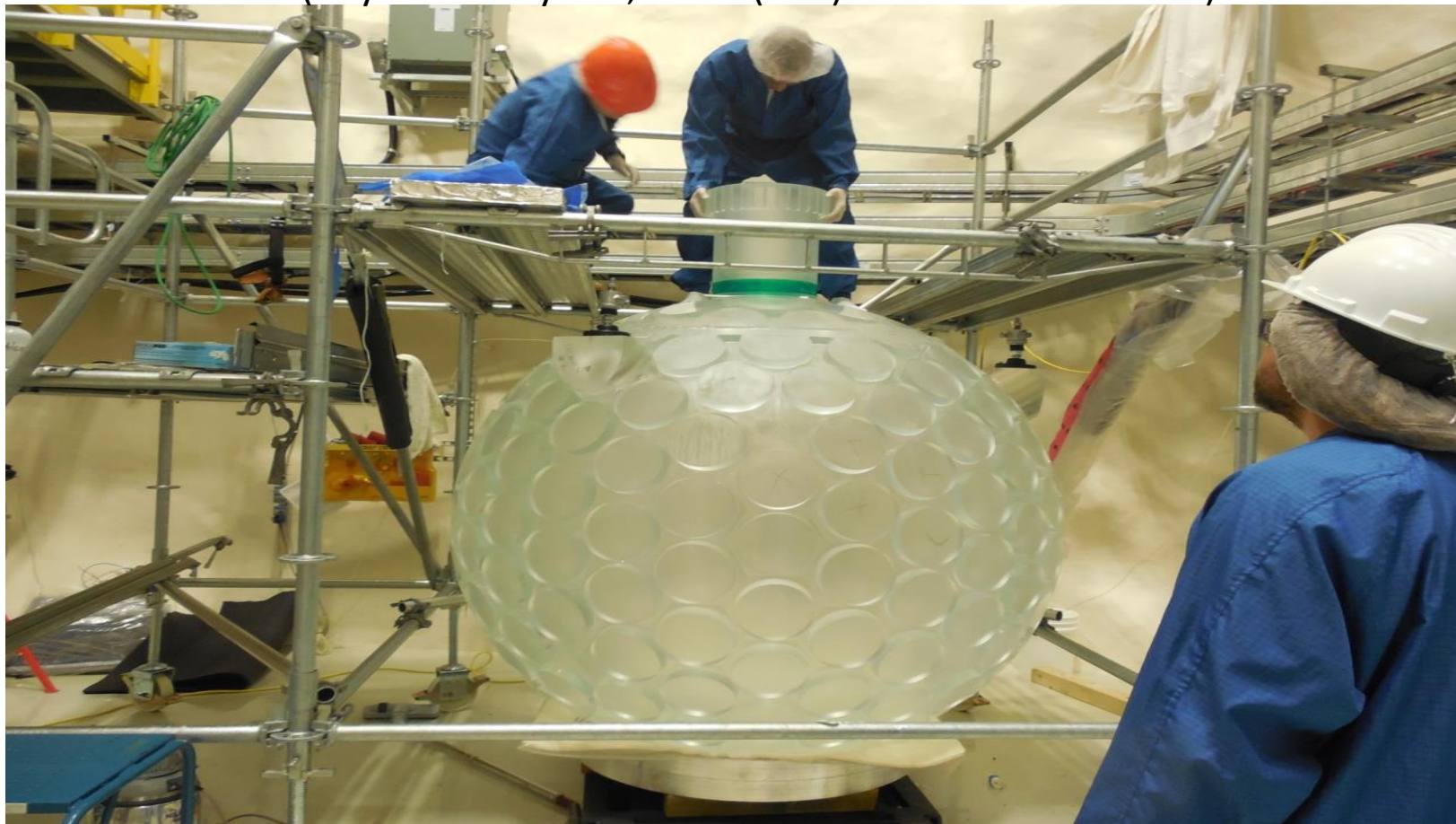
The AV neck is machined.



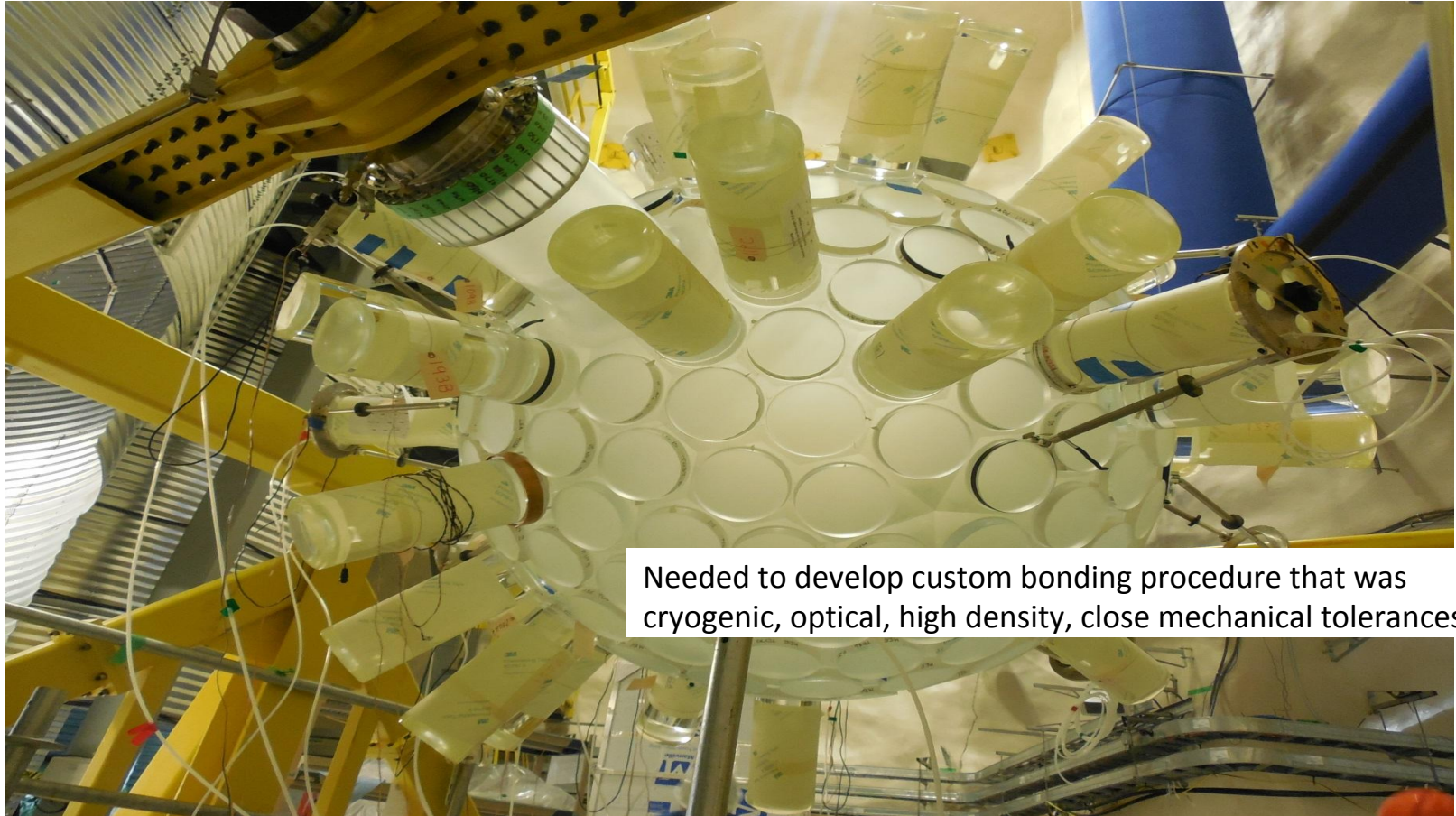
2" thick shell controls thermal stress. Stubs move bond to low stress regions.



AV Neck Bond (Reynolds Polymer, Tech. (RPT) at SNOLAB Jan 2013)



Vessel sealed and purged, approx. 50 LGs bonded (September 2013)

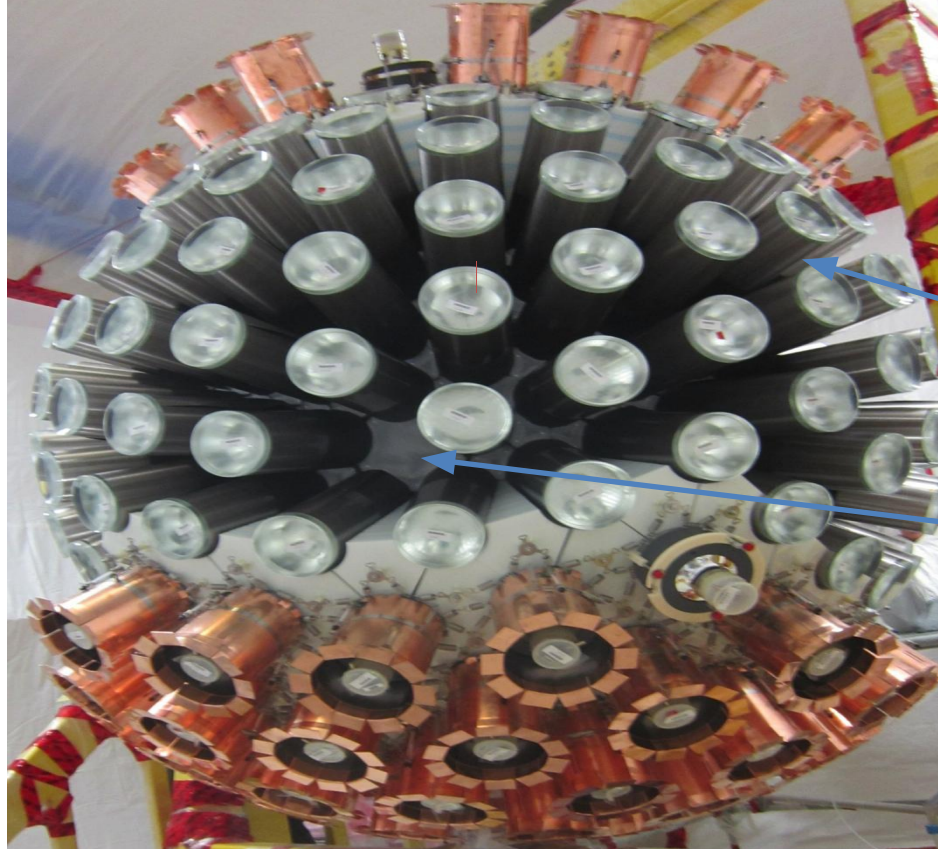
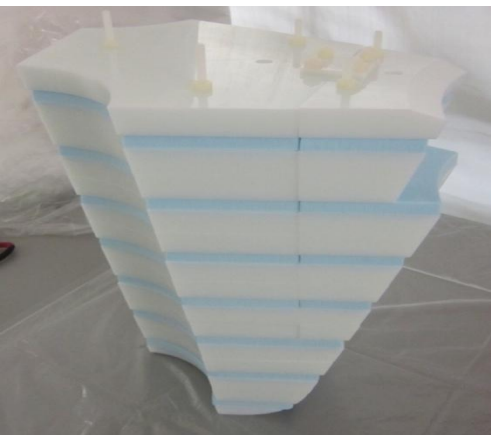


Needed to develop custom bonding procedure that was cryogenic, optical, high density, close mechanical tolerances.

Bonded underground, finish machined and then light guides attached:



November,  
2013

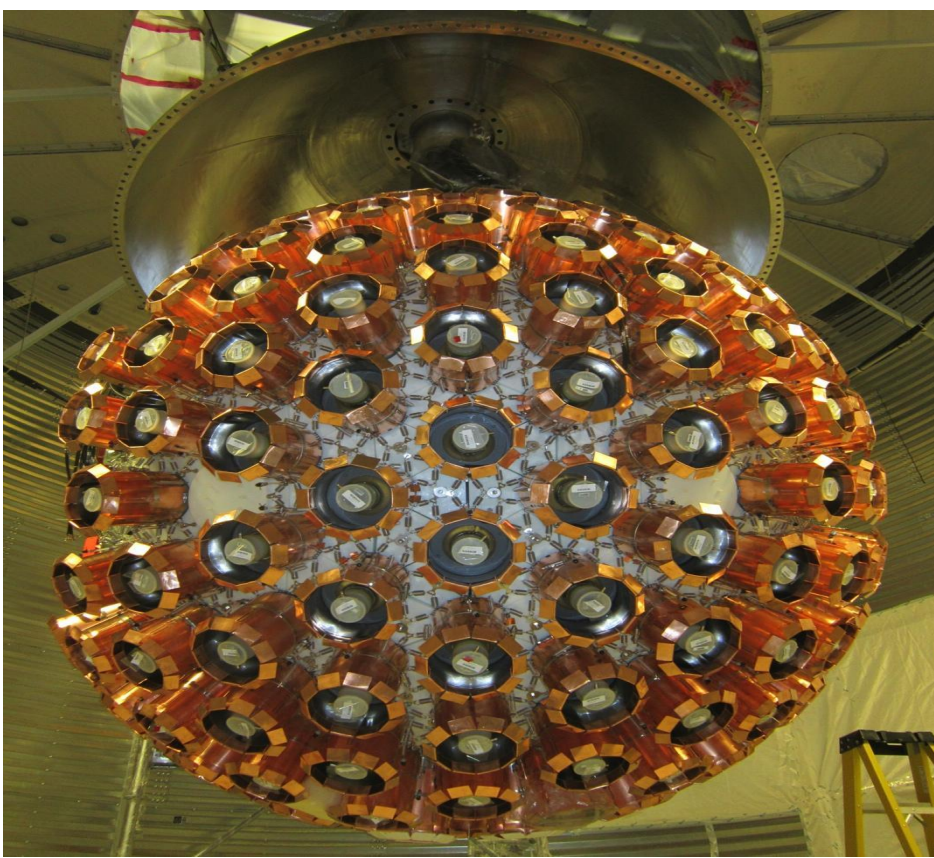


Specular  
reflectors

Diffuse  
reflectors

## Background suppression

- Assayed Polyethylene (white) & Styrofoam (blue)
- Neutron shielding (PMTs)



## Background suppression

- 50 cm of plastic shield
- $2.6 \times 10^5 \text{ n} \rightarrow 0.14 \text{ n}$  (in ROI)

## Maximum light detection

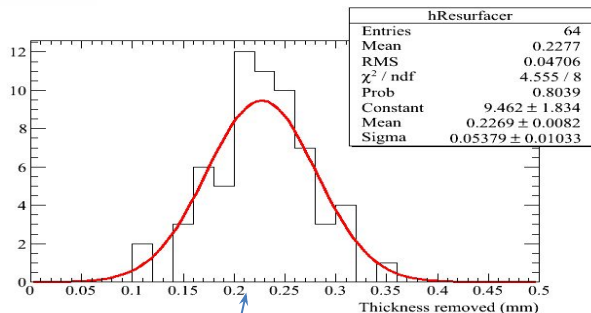
- Hamamatsu R5912 HQE  
(32% QE)

# DEAP-3600 Acrylic Vessel Resurfer

Removes  $\sim 1$  mm acrylic  
in-situ after construction

Radon-scrubbed  $N_2$   
purge gas and UPW  
flushing to extract  
residue

Surface contamination



24% uniformity demonstrated



# $4\pi$ TPB (Organic WLS) deposition source developed for DEAP-3600

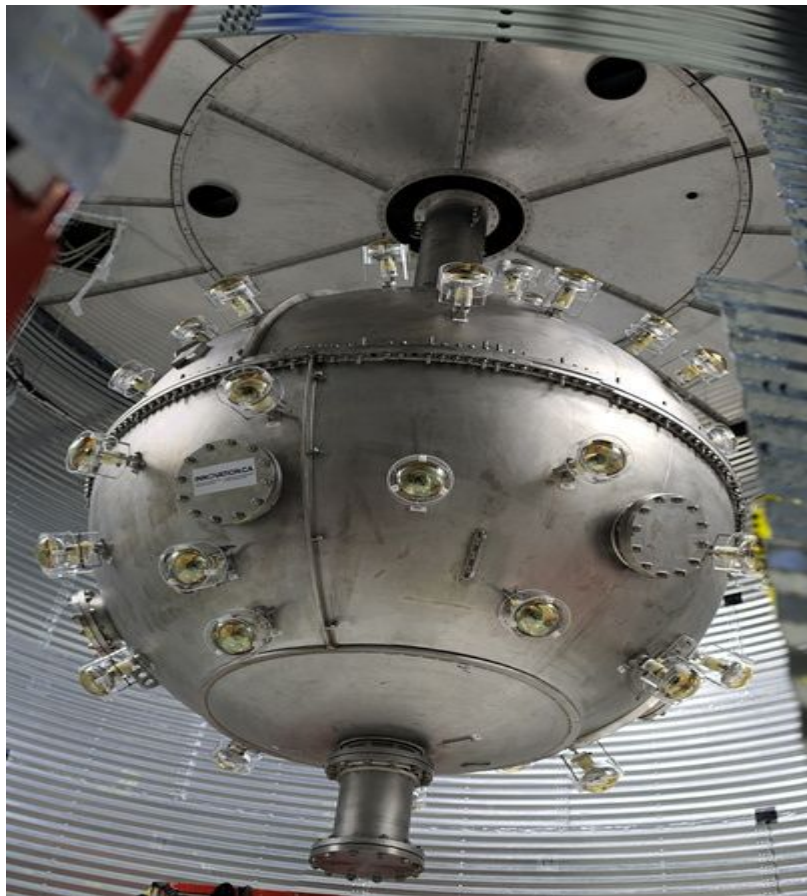


20-inch test vessel, 1/3 scale



Pula, 2017





Pula, 2017

# Liquid Argon Target Transfer



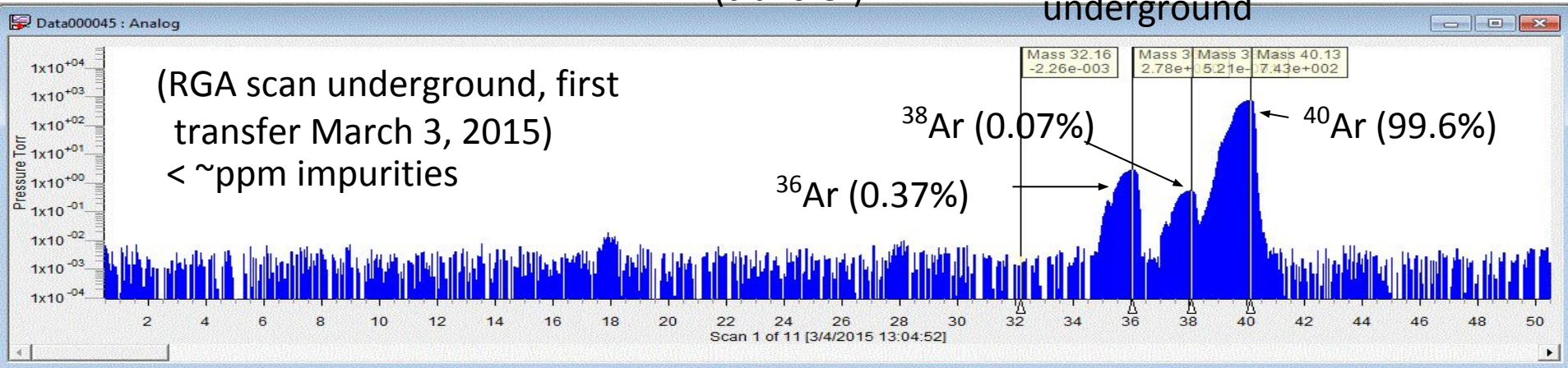
Bulk LAr storage on surface



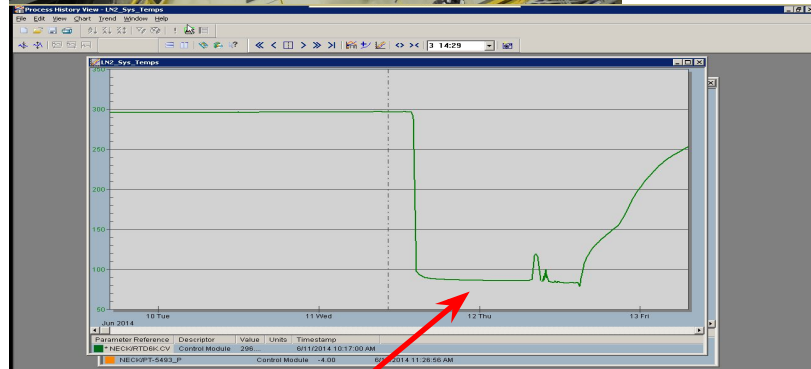
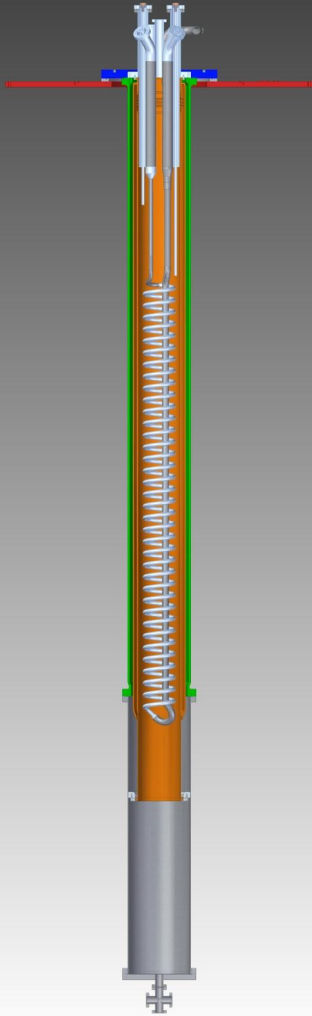
2x240L  
(transfer)



LN<sub>2</sub>-cooled storage dewar  
underground



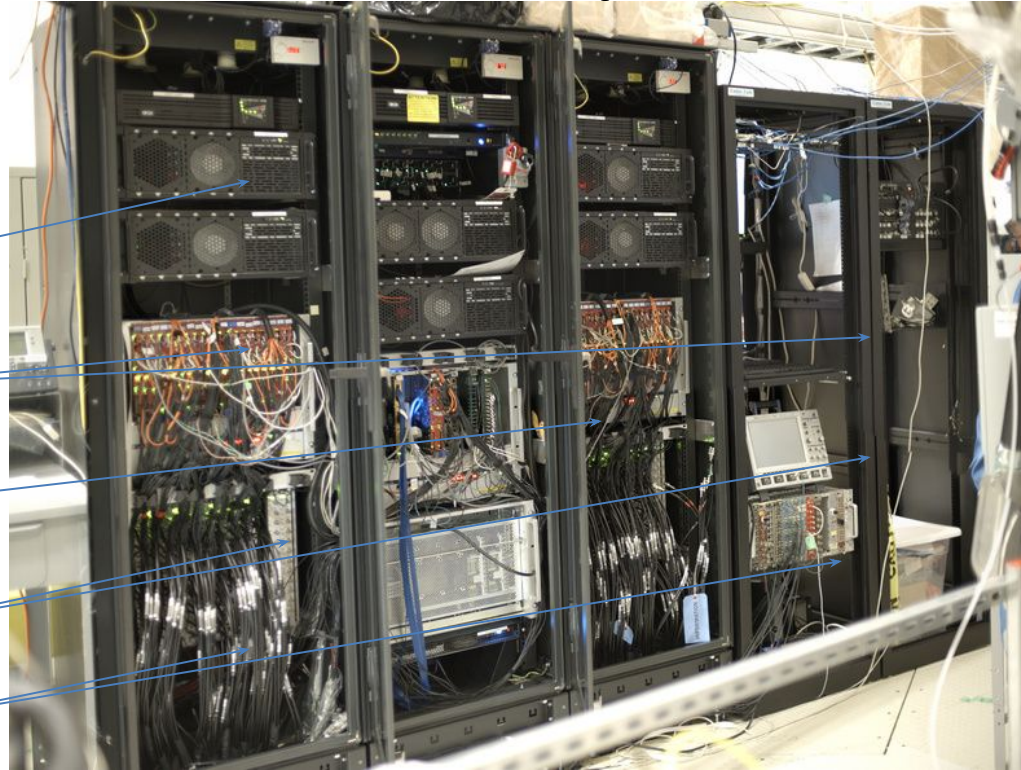
# DEAP-3600 Argon Cooling System



Commissioning at 86K, June 11 2014

LN2 system operating with cryogen since June 2014

# Electronics/DAQ



Front End Computers

CAEN V1720/V1740  
Digitizers

Digital Trigger Module

Signal conditioning  
boards

Cables from PMTs

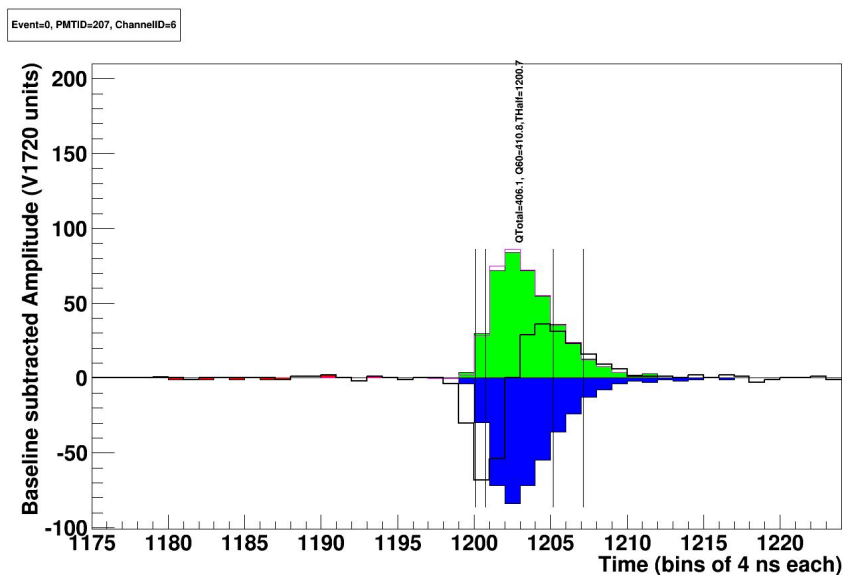
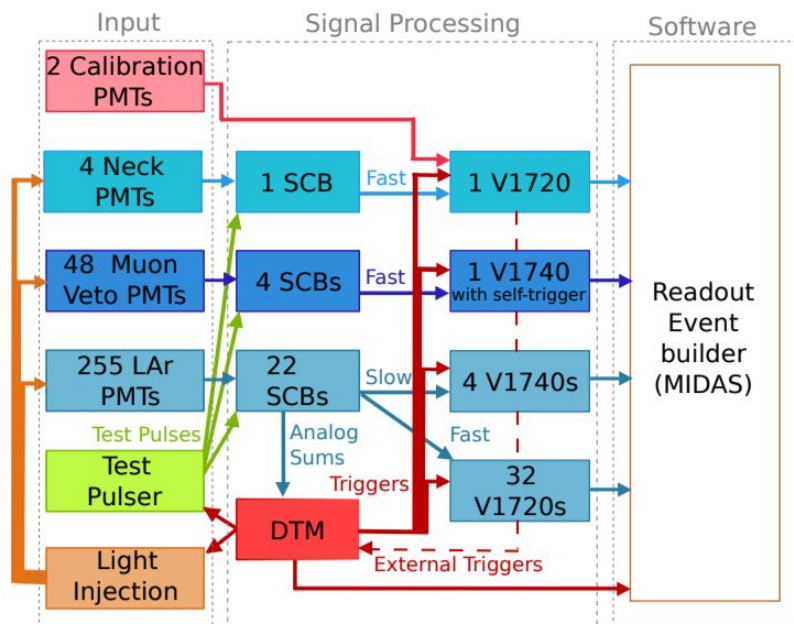
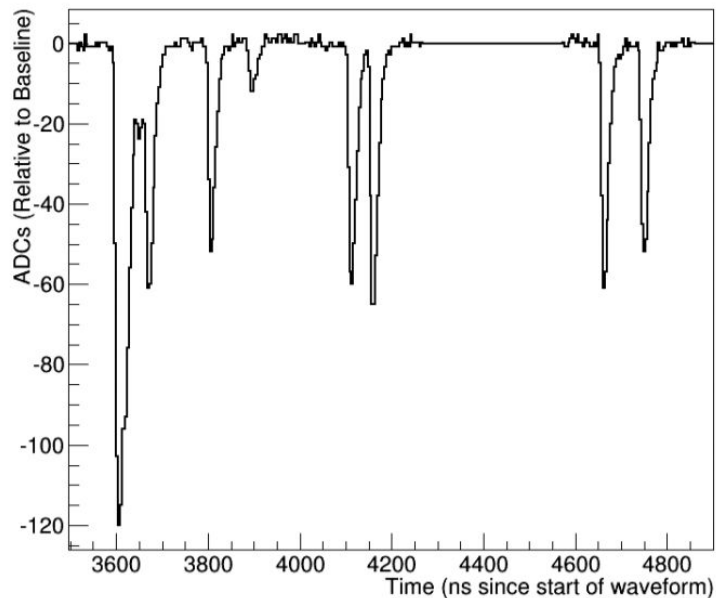
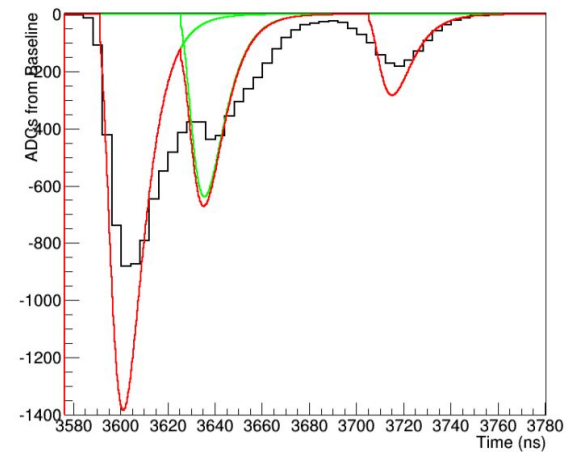


FIG. 2. A block diagram of the DEAP-3600 data acquisition system, adapted from [10]. Shown are the PMTs, the digitizer and trigger module (DTM), the signal conditioning boards (SCBs), the event builder, the light injection system, the test pulser systems, the fast high-gain channel digitizers (V1720s), and the slow low-gain channel digitizers (V1740s).

## From digitized waveforms to charges and times

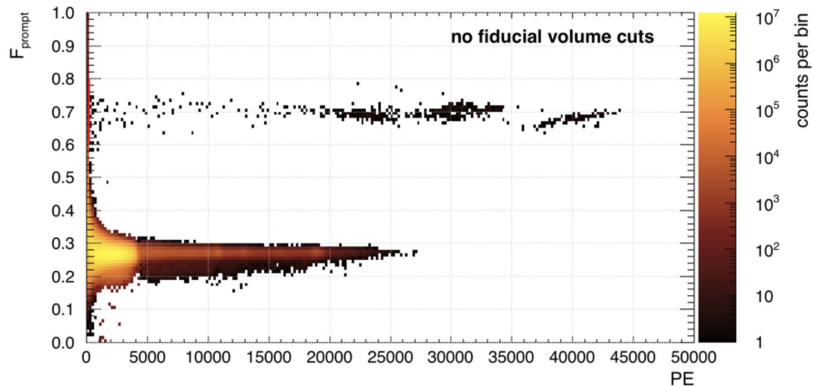


**Figure 5.1:** Example waveform for a single PMT in an event. Data is in ZLE mode, so only blocks of data that cross the digitizer's threshold of  $\sim 0.1$  of the mean PE amplitudes are shown.



**Figure 5.5:** Example of a large pulse where the sub-peaks are not fit, instead the sub-peaks are given the charge of the pulse integrals from valley-to-valley.

Most of the data are  $^{39}\text{Ar}$



What is each region in the plot?

$$F_{\text{prompt}} = \frac{\sum_{t=-28 \text{ ns}}^{60 \text{ ns}} \text{PE}(t)}{\sum_{t=-28 \text{ ns}}^{10 \text{ }\mu\text{s}} \text{PE}(t)}. \quad (1)$$

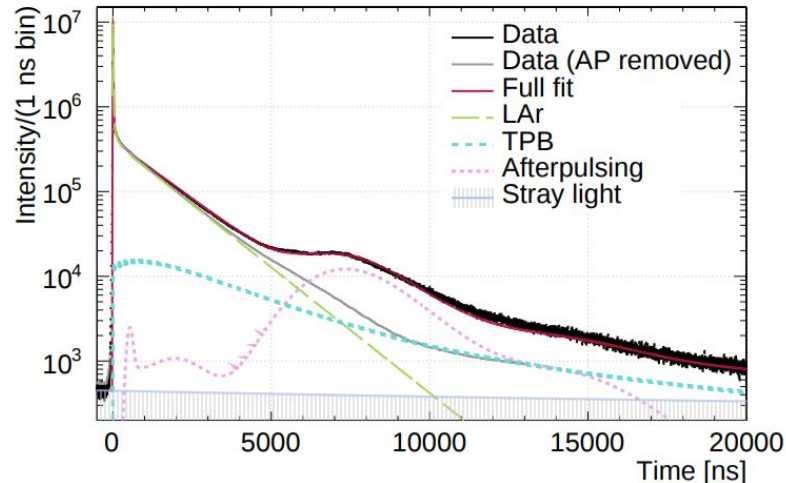


FIG. 3. Average  $^{39}\text{Ar}$  pulse shape before correction of instrumental effects (black) shown together with a model fit (red). The fit accounts for the following effects, which are shown individually: LAr singlet, triplet, and intermediate [23] light emission (green dashed), TPB prompt and delayed light emission [24] (blue dash-dotted), afterpulsing following all the previous components (pink dotted), and stray light (grey filled), which accounts for dark noise and the delayed TPB emission from previous events. The pulse shape made from pulses that use the pulse-by-pulse AP removal algorithm (see text) is also shown (grey solid).

To mimic the Wimp signal,  
we can use AmBe neutron  
source.

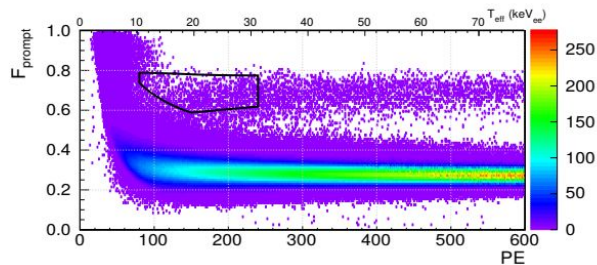


FIG. 3: AmBe source data after cuts, with the WIMP search ROI (black box).

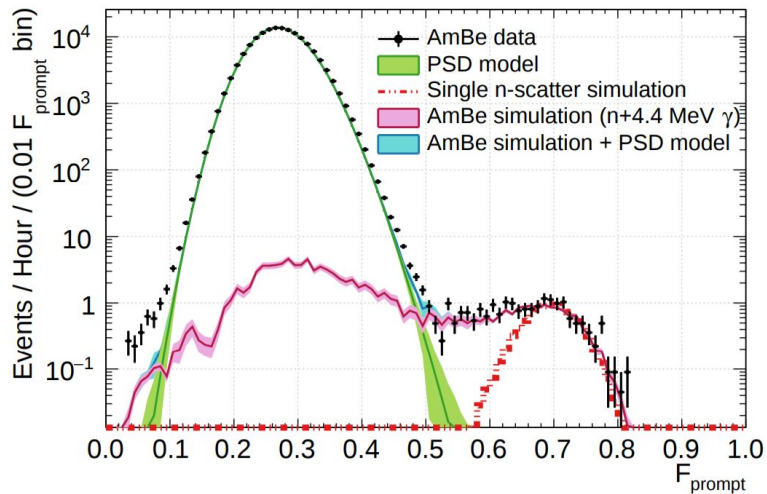


FIG. 8.  $F_{\text{prompt}}$  distribution in the 120–200 PE range of events from AmBe data (black) and simulations of single-scatter neutrons (red dashed). Also shown are simulated events from an AmBe source (pink), the ER PSD model (green) and their sum (blue).

Position Reconstruction: How do you extract a position from  $q, t$  of pulses

$$\ln \mathcal{L}(\vec{x}) = \sum_{i=1}^{N_{\text{PMTs}}} \ln \text{Poisson}(q_i; \lambda_i), \quad (6)$$

$$\lambda_i = \lambda_i \left( |\vec{x}|, \frac{\vec{x} \cdot \vec{r}_i}{|\vec{x}| |\vec{r}_i|}, q_{\text{total}} \right),$$

$$\ln \mathcal{L}(t_0, \vec{x}_0) = \sum_{i=1}^{N_{\text{PE}}} \ln \mathcal{L}^{t \text{ res.}}(t_i - t_0; \vec{x}_0, \text{PMT}_i),$$

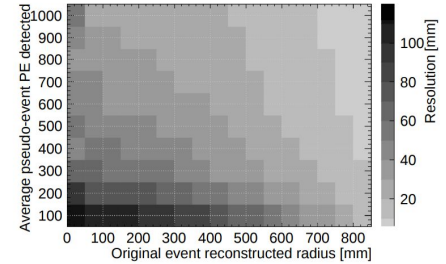


FIG. 10. Position resolution evaluated using the data-driven pseudo-event method, as a function of the average number of PE in both pseudo-events and the reconstructed radius drawn from the same original event, as returned by the PE-based algorithm. The  $z$ -axis scale denotes the resolution, defined as the characteristic width of the distribution of distances between reconstructed pseudo-events drawn from the same original event.

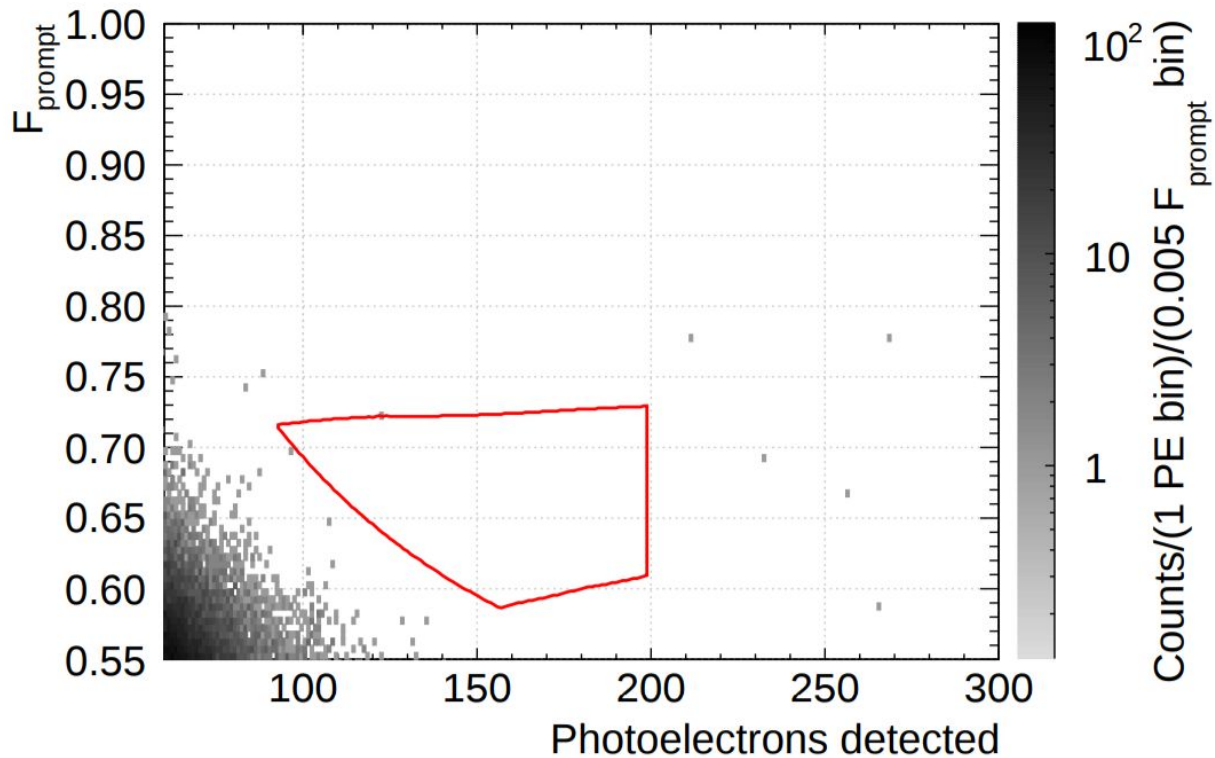


FIG. 21. Observed  $F_{\text{prompt}}$  vs. PE distribution after all cuts. The region of interest is shown in red.

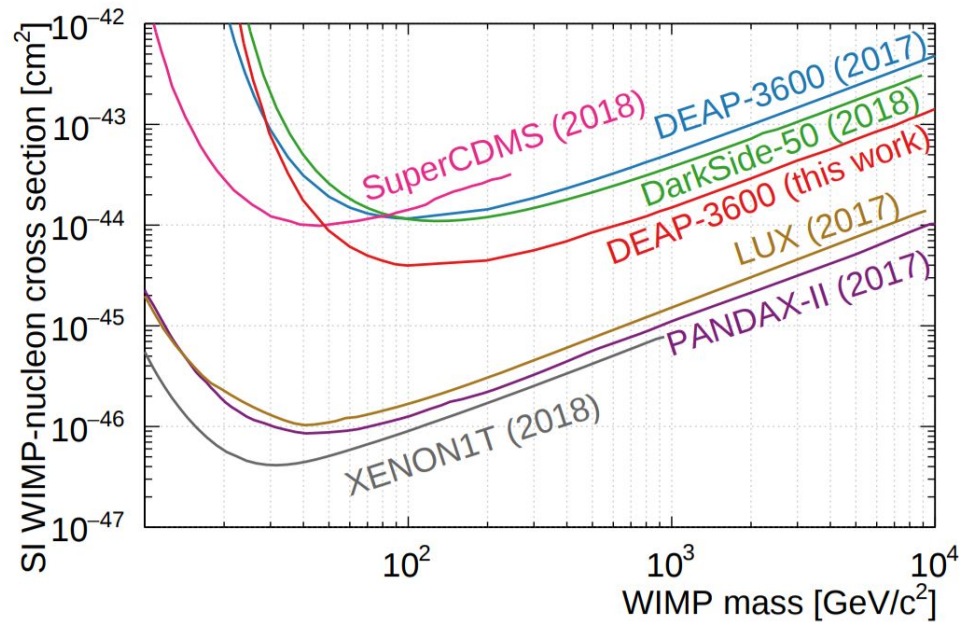


FIG. 23. 90% confidence upper limit on the spin-independent WIMP-nucleon cross sections based on the analysis presented in this paper (blue), compared to other published limits, including our previous limit [6], SuperCDMS [42], DarkSide-50 [7], LUX [43], PANDAX-II [44], and XENON1T [5].

Darkside 20k and Argo (300 Mg of LAr)

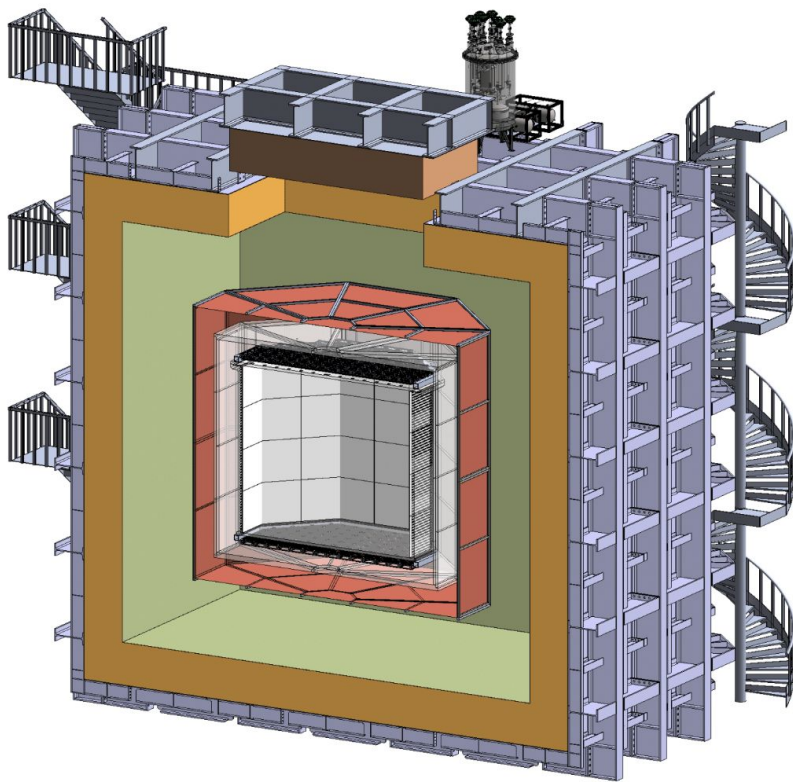


FIG. 1. Drawing of the DS-20k detector: the PMMA TPC filled with UAr surrounded by the veto detector made of a Gd-loaded PMMA shell between two AAr active layers, all contained within a membrane cryostat. The outer active argon layer is optically separated from the AAr by a membrane. For clarity, the mechanical supports holding the veto and TPC are not shown.

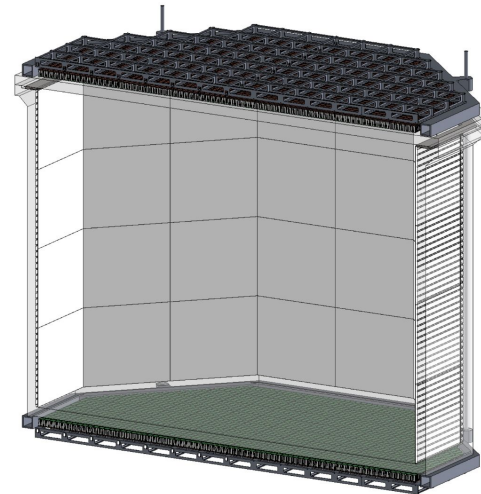


FIG. 2. Drawing of the DarkSide-20k LAr TPC, detailing the PMMA sealed vessel, TPC field cage, and PDMs support structure. For clarity, the mechanical supports holding the TPC and many other engineering details are not shown.

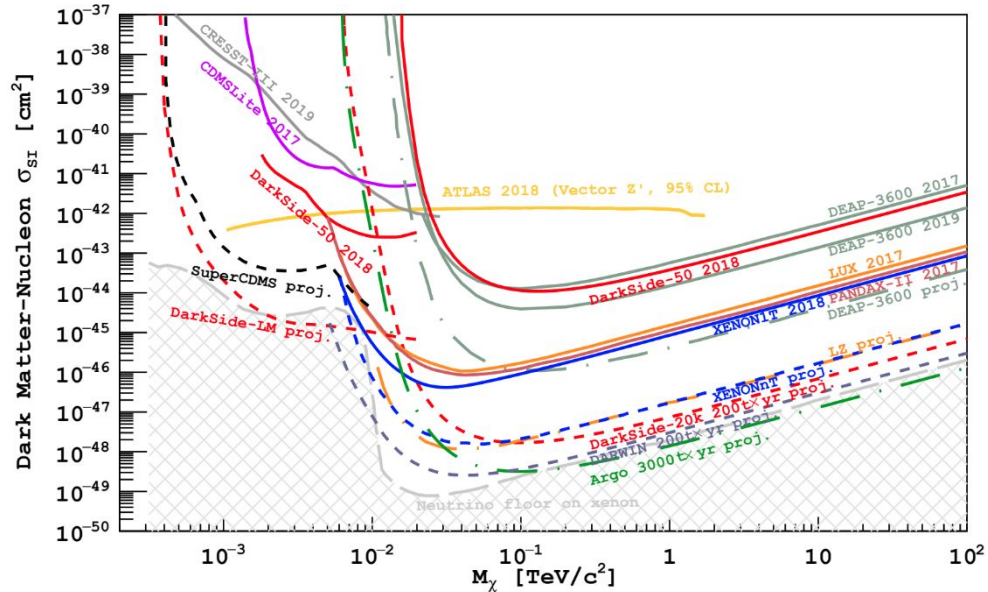


FIG. 3. 90% C.L. exclusion limits showing leading results from direct (continuous lines, Ref. [6, 7, 12–15]) and accelerator-based dark matter searches (region above the yellow line [16]) compared with sensitivities of future germanium-, xenon-, and argon-based direct searches (dashed lines, Ref. [17–21] and this work). The “neutrino floor” curve follows the definition of Ref. [22]. The 95% C.L. limit from the ATLAS Experiment is shown for a benchmark model in which Dirac-fermion WIMPs interact with ordinary matter via a vector mediator with coupling strengths to quarks, leptons and WIMPs of 0.25, 0.01, and 1, respectively [23].

# DEAP Collaboration

## University of Alberta

**D. Grant**, **P. Gorel**, **A. Hallin**, J. Soukup, C. Ng, **B. Beltran**, K. Olsen, R. Chouinard, T. McElroy, S. Crothers, S. Liu, P. Davis, and A. Viangreiro

## Carleton University

**K. Graham**, **C. Ouellet**, Carl Brown

## Queen's University

**M. Boulay**, **B. Cai**, D. B. Broerman, Bearse, J. Bonnat, K. Dering, **M. Chen**, S. Florian, R. Gagnon, **V.V. Golovko**, P. Harvey, **M. Kuzniak**, **A. McDonald**, C. Nantais, **A.J. Noble**, E. O'Dwyer, P. Pasuthip, L. Veloce, **W. Rau**, **T. Sonley**, **P. Skensved**, **M. Ward**

## SNOLAB/Laurentian

**B. Cleveland**, **F. Duncan**, **R. Ford**, **C.J. Jillings**, **T. Pollmann**, **C. Stone**

## SNOLAB

I. Lawson, K. McFarlane, P. Liimatainen, O. Li

## TRIUMF

**F. Retiere**, **Alex Muir**, P-A. Amaudruz, D. Bishop, S. Chan, C. Lim, C. Ohlmann, K. Olchanski, V. Strickland

## National Autonomous University of Mexico

**E. Vazquez Jauregui**

## Rutherford Appleton Laboratory

**P. Majewski**

## Royal Holloway University of London

**J. Monroe**, **J. Walding**, A. Butcher

## University of Sussex

**Simon Peeters**

